



1 **Enhanced heterogeneous uptake of sulfur dioxide on**
2 **mineral particles through modification of iron speciation**
3 **during simulated cloud processing**

4 **Zhenzhen Wang¹, Tao Wang¹, Hongbo Fu^{1, 2, 3}, Liwu Zhang¹, Mingjin Tang⁴,**
5 **Christian George⁵, Vicki H. Grassian⁶, and Jianmin Chen¹**

6 ¹Shanghai Key Laboratory of Atmospheric Particle Pollution and Prevention,
7 Department of Environmental Science & Engineering, Institute of Atmospheric
8 Sciences, Fudan University, Shanghai, 200433, China

9 ²Shanghai Institute of Pollution Control and Ecological Security, Shanghai 200092,
10 China

11 ³Collaborative Innovation Center of Atmospheric Environment and Equipment
12 Technology (CICAEET), Nanjing University of Information Science and Technology,
13 Nanjing 210044, China

14 ⁴State Key Laboratory of Organic Geochemistry and Guangdong Key Laboratory of
15 Environmental Protection and Resources Utilization, Guangzhou Institute of
16 Geochemistry, Chinese Academy of Sciences, Guangzhou 510640, China

17 ⁵University of Lyon, Université Claude Bernard Lyon 1, CNRS, IRCELYON,
18 F-69626, Villeurbanne, France

19 ⁶Departments of Chemistry and Biochemistry, University of California, San Diego, La
20 Jolla, California 92093, United States

21 *Correspondence to:* Hongbo Fu (fuhb@fudan.edu.cn); Jianmin Chen
22 (jmchen@fudan.edu.cn)

23



24 **Abstract.** Iron-containing mineral aerosols play a key role in the oxidation of sulfur
25 species in the atmosphere. Simulated cloud processing (CP) of typical mineral
26 particles, such as illite (IMt-2), nontronite (NAu-2), smectite (SWy-2) and Arizona
27 test dust (ATD) is shown here to modify sulfur dioxide (SO₂) uptake onto mineral
28 surfaces. Heterogeneous oxidation of SO₂ on particle surfaces was firstly investigated
29 using an *in situ* DRIFTS apparatus. Our results showed that the BET surface area
30 normalized uptake coefficients (γ_{BET}) of SO₂ on the IMt-2, NAu-2, SWy-2 and ATD
31 samples after CP were 2.2, 4.1, 1.5 and 1.4 times higher than the corresponding ones
32 before CP, respectively. The DRIFTS results suggested that CP increased the amounts
33 of reactive sites (e.g., surface OH groups) on the particle surfaces and thus enhanced
34 the uptake of SO₂. TEM showed that the particles broke up into smaller pieces after
35 CP, and thus produced more active sites. The “free-Fe” measurements confirmed that
36 more reactive Fe species were present after CP, which could enhance the SO₂ uptake
37 more effectively. Mössbauer spectroscopy further revealed that the formed Fe phase
38 were amorphous Fe(III) and nanosized ferrihydrite hybridized with Al/Si, which were
39 possibly transformed from the Fe in the aluminosilicate lattice. The modification of
40 Fe speciation was driven by the pH-dependent fluctuation coupling with Fe
41 dissolution-precipitation repeatedly during the experiment. Considering both the
42 enhanced SO₂ uptake and subsequent promotion of iron dissolution along with more
43 active Fe formation, which in turn lead to more SO₂ uptake, it was proposed that there
44 may be a positive feedback between SO₂ uptake and iron mobilized on particle
45 surfaces during CP, thereby affecting climate and biogeochemical cycles. This
46 self-amplifying mechanism generated on the particle surfaces may also serve as the
47 basis of high sulfate loading in severe fog-haze events observed recently in China.

48



49 **1 Introduction**

50 Mineral dust is a major fraction of global atmospheric aerosol budget, with an
51 estimated annual emission flux of 1000 to 3000 Tg into the atmosphere (Jickells et al.,
52 2005; Andreae and Rosenfeld, 2008). Mineral dust aerosol mainly consists of quartz,
53 feldspars, carbonates (calcite, dolomite), and clay minerals (illite, kaolinite, chlorite,
54 montmorillonite), the exact composition varies with source (Claquin et al., 1999;
55 Formenti et al., 2008). During the long-range transport, mineral dust provides a
56 reactive surface for heterogeneous chemistry (Zhang et al., 2006; George et al., 2015;
57 Huang et al., 2015). Heterogeneous reactions of atmospheric trace gases on mineral
58 dust particles are of great significance as these reactions alter the chemical balance of
59 the atmosphere and modify the properties of individual particles (Usher et al., 2003;
60 Wu et al., 2011; Huang et al., 2015).

61 SO₂ is an important trace gas, which is released mainly by fossil fuel combustion
62 and volcanic emission. The heterogeneous conversion of SO₂ on mineral dust surfaces
63 leads to the formation of sulfuric acid and sulfate aerosols, resulting in a significant
64 cooling effect on the global climate by scattering solar radiation and acting as cloud
65 condensation nuclei (CCN) to affect climate indirectly (Lelieveld and Heintzenberg,
66 1992; Usher et al., 2003; Kolb et al., 2010). In addition, sulfate containing particles
67 play a significant role in the haze formation in China in recent years (Sun et al., 2014;
68 Wang et al., 2014; Yang et al., 2017). SO₂ can be gaseous oxidized to sulfate by OH
69 radical, and be aqueous oxidation in cloud and fog droplets by ozone and hydrogen
70 peroxide (Luria and Sievering, 1991), or through heterogeneous processes that occur
71 on aerosol particle surfaces (Usher et al., 2003; Ullerstam et al., 2003). However, the
72 high sulfate levels measured in recent field observations cannot be explained by
73 current atmospheric models (Kerminen et al., 2000; Wang et al., 2003; Cheng et al.,



74 2016), leading to a large gap between the modeled and field-observed sulfate
75 concentrations using known oxidation pathways (Herman, 1991; Kasibhatla et al.,
76 1997; Barrie et al., 2016). Overall, on a global scale, atmospheric SO₂ concentration
77 were typically overestimated, while sulfate tended to be underestimated, suggesting
78 missing sulfate production pathways (Harris et al., 2013; Kong et al., 2014).

79 It has been suggested that the heterogeneous conversion of SO₂ could make an
80 important contribution to the atmospheric sulfate loading. Laboratory studies typically
81 focus on SO₂ uptake onto a variety of metal oxides and mineral particles (Goodman et
82 al., 2001; Usher et al., 2002; Zhao et al., 2015; Yang et al., 2016), and have confirmed
83 that its conversion rate on the surface of Fe (hydr)oxides was faster compared to other
84 metal oxides investigated, in good agreement with the field-measurement (Usher et al.,
85 2002; Zhang et al., 2006). Atmospheric Fe is emitted from both anthropogenic
86 (primarily biomass burning, coal and oil combustion) and natural (mineral dust and
87 volcanic ash) sources, with the mineral dust source dominant globally (Siefert et al.,
88 1998; Luo et al., 2008). It has been established that an important in cloud S (IV)
89 oxidation pathway is catalyzed by natural transition metal ions, especially Fe hosted
90 within mineral particles (Alexander et al, 2009; Harris et al., 2013; Ito et al., 2019).

91 Another important consideration for heterogeneous chemistry of mineral dust
92 aerosol, is how mineral dust particles change in the atmosphere. During long-range
93 transport, mineral particles often undergo chemical ageing by atmospheric processes
94 (Mahowald et al., 2005; Baker and Croot, 2010; Shi et al., 2011). Cloud processing
95 involves cloud water condensation and evaporation on the particle surfaces, along
96 with drastic liquid water content and pH fluctuations (Mackie, 2005; Shi et al., 2011;
97 Rubasinghege et al., 2016). During CP, the high relative humidity (RH) results in high
98 aerosol water content and relatively high pH (Behra et al., 1989; Baker and Croot,



99 2010; Shi et al., 2011). While water evaporation from cloud droplets to wet aerosol at
100 higher temperature, the particles only contain a concentrated aqueous aerosol solution,
101 in which the pH can be lower than 2 (Zhu et al., 1993; Meskhidze, 2003; Shi et al.,
102 2015). Therefore, there is a highly acidic film (e.g., pH = 2) in the “wet aerosol” phase
103 versus a less acidic droplet (near-neutral, 5-6) in the “cloud droplet” phase within
104 clouds (Shi et al., 2015). During its lifetime, a typical aerosol particle may experience
105 several cloud cycles involving large pH variations before being removed from the
106 atmosphere as rain or through dry deposition (Pruppacher and Jaenicke, 1995; Maters
107 et al., 2016). Herein, the simulated CP experiment was conducted by changing pH
108 between 2 and 5-6, in accordance with the previous studies (Spokes et al., 1994;
109 Mackie, 2005; Shi et al., 2009).

110 It was well documented that pH is especially important for Fe mobilization (Zhu et
111 al., 1993; Desboeufs et al., 2001; Deguillaume et al., 2010; Maters et al., 2016). The
112 fluctuating pH during CP will impact and change the Fe speciation and morphology in
113 dust particles (Zhuang et al., 1992; Wurzler et al., 2000; Shi et al., 2009; Kadar et al.,
114 2014). The low pH will increase Fe solubility and bioavailability of dust during
115 transport, thereby providing Fe external input to the open ocean surface to promote
116 marine prime productivity (Spokes et al., 1994; Desboeufs et al., 2001). It has been
117 found that Fe-rich nanoparticle aggregates were formed from Saharan soil and
118 goethite upon simulated CP conditions, in good agreement with their
119 field-measurements from the wet-deposited Saharan dusts collected from the western
120 Mediterranean (Shi et al., 2009). Fe nanoparticles are more chemically reactive
121 (Wurzler et al., 2000; Desboeufs et al., 2001), possibly lead to a remarkable difference
122 in heterogeneous chemistry. However, little is known about the influence of CP on
123 SO₂ uptake onto particle surfaces up to now.



124 In this study, we employed four typical mineral samples as surrogates to perform
125 simulated CP experiments. The SO₂ uptakes on the mineral particles before and after
126 CP were compared using *in situ* diffuse reflectance infrared Fourier transform
127 spectroscopy (DRIFTS). Transmission electron microscopy (TEM) was applied to
128 observe the morphological and mineralogical change of mineral particles. The Fe
129 speciation modification during simulated CP was further monitored by the dissolved
130 Fe measurement, the “free-Fe” analysis and Mössbauer spectroscopic
131 characterization.

132 2 Material and methods

133 2.1 Mineral particles

134 The standard mineral samples of IMt-2, NAu-2 and SWy-2 were purchased from
135 the Source Clay Minerals Repository (Purdue University, West Lafayette, IN). ATD
136 was purchased from Powder Technology Inc. (Burnsville, MN, USA). The mineral
137 samples were coarsely ground using a mortar and pestle before being more finely
138 ground using an All-dimensional Planetary Ball Mill QM-QX (Nanjing University
139 Instrument Plant) and were sieved to particle diameters (D_p) < 45 μm prior to analysis.
140 The Brunauer-Emmett-Teller specific surface areas (S_{BET}) of the samples were
141 measured with a Quantachrome Nova 1200 BET apparatus. Total iron content (Fe_T) of
142 the samples were determined using an inductively coupled plasma atomic emission
143 spectroscopy (ICP-AES, Jobin Yvon Ultima). The chemical compositions of the
144 particles were analyzed by X-ray fluorescence spectrometry (XRF, PANalytical Axios
145 Advanced).

146 2.2 Cloud processing simulation experiment

147 The simulated CP experiments were conducted at a constant temperature ($298 \pm 1\text{K}$)
148 using a Pyrex glass vessel with a water jacket. The suspensions contained a mineral



149 particle loading of 1 g L^{-1} were subjected to acidic ($\text{pH} = 2 \pm 0.1$, 24 h) and
150 near-neutral pH ($\text{pH} = 5\text{-}6$, 24 h) cycles for 1-3 times according to the previous
151 methods (Spokes et al., 1994; Mackie, 2005; Shi et al., 2009). The suspension pH was
152 adjusted by adding dilute H_2SO_4 or NH_4OH . The CaCO_3 equivalent alkalinity of the
153 dust was determined in accordance with APHA method 2320B so that acid additions
154 to control pH could be adjusted accordingly (Mackie, 2005). The amount of acid or
155 alkali added to achieve these pH cycles was less than 1% of the total volume of the
156 suspensions. The experiments were performed under a constant stirring (about 50
157 rpm) in the dark for 144 h. At the end of the CP experiment, the suspensions were
158 filtered through $0.2 \mu\text{m}$ PTFE filters (Millipore). The filter residue was air-dried, and
159 was further applied to the DRIFTS experiment, as well as TEM observation, “free-Fe”
160 measurement and Mössbauer spectroscopic characterization.

161 **2.3 SO_2 uptake on the mineral particles**

162 The SO_2 uptake on the particle surfaces before and after CP was investigated by a
163 Shimadzu Tracer-100 FTIR spectrometer equipped with a high-sensitivity mercury
164 cadmium telluride (MCT) detector and a diffuse reflectance accessory. A temperature
165 controller was fitted to the DRIFTS chamber to ensure constant reaction temperature
166 (298 K). Weighted sample was placed into a ceramic crucible (0.35 mm depth, 5 mm i.
167 d.) in the chamber. Mass flow controllers (Beijing Sevenstar electronics Co., LTD)
168 were used to adjust the reactant gases to a flux with expected concentration and
169 relative humidity. The sample was firstly pretreated in a 100 mL min^{-1} flow of
170 synthetic air (21% O_2 and 79% N_2) for 1 h to blow off water and impurities on
171 particle surface. When the background spectrum of the fresh sample reached steady
172 state, the reactant gas of SO_2 (5.0 ppm) along with synthetic air was introduced into
173 the chamber at a total flow rate of 120 mL min^{-1} for 45 min, during which the IR



174 spectrum was recorded automatically every 5 min at a resolution of 4 cm⁻¹ for 100
175 scans in the spectral range of 900 to 4000 cm⁻¹. Atmospheric moisture was simulated
176 with a RH level around 40 % by guiding one high-pure air flux through water. The
177 humidity value was monitored using a hygrometer.

178 The sulfate products were analyzed by ion chromatography (IC) after the DRIFTS
179 experiments. The particles were extracted with 5 ml ultrapure water by ultrasonic
180 extractor. After 10 min, the extracted solution was passed through a 0.22 μm PTFE
181 membrane filter and the leaching solution was analyzed using a Metrohm 883 Basic
182 IC equipped with an A5-250 column. A weak base eluent (3.2 mmol L⁻¹ Na₂CO₃ plus
183 1.0 mmol L⁻¹ NaHCO₃) was used for anion detection at a flow rate of 0.70 ml min⁻¹.
184 To discriminate the adsorbed sulfate during simulated CP experiment and the sulfate
185 ions generated from the heterogeneous reaction, the adsorbed sulfate on the particles
186 during simulated CP experiment were initially measured as blank. The heterogeneous
187 uptake of SO₂ was calculated by subtracting the blank value from the total sulfate
188 ions.

189 The reactive uptake coefficient (γ) was defined as the rate of sulfate formation on
190 the surface ($d[\text{SO}_4^{2-}]/dt$, ions s⁻¹) divided by collision frequency (Z , molecules s⁻¹)
191 (Usher et al., 2003; Ullerstam et al., 2003; Kong et al., 2014; Huang et al., 2015).

$$192 \quad \gamma = \frac{d[\text{SO}_4^{2-}]/dt}{Z}, \quad (1)$$

$$193 \quad Z = \frac{1}{4} \times A_s \times [\text{SO}_2] \times v, \quad (2)$$

$$194 \quad v = \sqrt{\frac{8RT}{\pi M_{\text{SO}_2}}}, \quad (3)$$

195 Where, A_s is the effective sample surface of the samples, m²; v is the mean
196 molecular velocity of SO₂, m s⁻¹; R is the gas constant, J mol K⁻¹; T is the absolute
197 temperature, K; and M_{SO_2} is the molecular weight of SO₂, kg mol⁻¹.



198 A conversion factor was obtained by a calibration plot with numbers of SO_4^{2-}
199 analyzed by ion chromatography (IC, Metrohm 883 Basic, Switzerland) versus the
200 integrated areas of sulfate products from DRIFTS spectra. The residual sulfate during
201 simulated CP experiments were deducted as background. The calculated conversion
202 factor of SO_4^{2-} is 1.170×10^{15} (ions \cdot integrated units $^{-1}$). Integrated areas for the total
203 sulfur-containing products were calculated to show the maximal sulfate formation
204 rates. The reactive uptake coefficient for SO_2 was determined to be γ_{BET} and γ_{geo} using
205 the BET area ($A_{\text{BET}} = \text{mass} \times S_{\text{BET}}$) and geometric area ($A_{\text{geo}} = \text{mass} \times S_{\text{BET}}$) as the
206 reactive area, respectively.

207 **2.4 Morphological and mineralogical characterization of the Fe speciation**

208 A FEI TECNAI G2 S-TWIN F20 TEM equipped with an Oxford energy-dispersive
209 X-ray spectrometer (EDX) was used to analyze the morphological and chemical
210 composition of individual particles before and after CP. Suspensions (0.2 g L^{-1}) of
211 each particle were prepared in methanol and sonicated for at least 1 h. A drop of this
212 suspension was then applied to a carbon-coated Cu TEM grid (400 mesh; EMS). A
213 FEI TECNAI G2 S-TWIN F20 TEM equipped with an Oxford energy-dispersive
214 X-ray spectrometer (EDX) was used for high-resolution imaging and to analyze the
215 chemical composition of individual particles. The Fe content of the typical individual
216 mineral particle were calculated from the values of 50 typical particles. Selected area
217 electron diffraction (SAED) was used to identify the crystalline phases.

218 The content of “free-Fe” in the mineral particles was determined by a
219 citrate-buffered-dithionite (CBD) sequential Fe extractions method according to the
220 literature (Lafon et al., 2004; Shi et al., 2009). Simply, 30 mg of the dust samples
221 were treated for 24 h with a 10 mL ascorbate solution ($\text{pH} = 7.5$) to extract chemically
222 highly labile Fe phases (Fe_A), mainly composed of amorphous, nanoparticle and/or



223 poorly crystalline ferrihydrite. The solutions were filtered through 0.2 μm
224 polycarbonate filters. The dust particles collected on the filters were subsequently
225 treated for 2 h with a 10 mL sodium dithionite solution ($\text{pH} = 4.8$) to extract
226 crystalline Fe (oxyhydr) oxides (Fe_D), which are mainly goethite and hematite. After
227 each reaction step, the dissolved Fe concentrations (Fe_A and Fe_D) in the filtrates were
228 determined using ICP-AES. The sum of these two pools ($\text{Fe}_A + \text{Fe}_D$) was defined as
229 the “free-Fe” fraction (Shi et al., 2011). The other fraction was donated as the
230 “structural-Fe” in aluminosilicate crystals, which could be calculated from the
231 difference between the Fe_T and “free-Fe” fractions (Lafon et al., 2004).

232 The Mössbauer spectroscopic analysis performed in transmission geometry with a
233 constant acceleration was used to inspect the chemical valence and the surrounding
234 structure of Fe in the particles before and after CP. ^{57}Co was used as the Mössbauer
235 source, and a 1 mm thick Na(Tl) scintillator coupled to a EMI9750B photoelectric
236 multiplier was used as the detector (Cwiertny et al., 2008). The measurement was
237 carried out at room temperature (RT) with a duration of 24 hours for one sample
238 (around 1.5×10^6 counts per channel). Experimental data were fitted by a least-squares
239 fitting-program. The isomer shift values were calibrated against a spectrum for α -Fe
240 metal foil.

241 During the simulated CP experiment, the total dissolved iron (Fe_s) and the dissolved
242 Fe(II) in the suspensions were measured colorimetrically by the Ferrozine method, as
243 described in previous studies (Viollier et al., 2000; Cwiertny et al., 2008). For Fe(II)
244 analysis, 200 mL of a 5 mM 1, 10-phenanthroline solution and 200 mL of an
245 ammonium acetate buffer were added into 1 mL of sample. To avoid possible
246 interference from Fe(III), which can also form a complex with 1,10-phenanthroline
247 when present at high concentrations, 50 mL of 0.43 M ammonium fluoride was added



248 to the sample prior to 1,10-phenanthroline. The mixture was allowed to sit in the dark
249 for 30 min prior to ultraviolet-visible spectroscopy (UV-Vis) analysis, during which
250 time a reddish-orange color developed if Fe(II) was present. Fe_s was determined via
251 the same protocol, except that 20 mL of 1.5 M hydroquinone, which reduces Fe(III) to
252 Fe(II), was added to the sample rather than ammonium fluoride. Absorbance
253 measured at 510 nm was converted to concentrations using aqueous standards
254 prepared from anhydrous beads of ferrous chloride. Standards were prepared in each
255 acid used in dissolution studies, and no matrix effects were observed. These
256 conditions resulted in a detection limit of 1 μM. The concentration of dissolved
257 Fe(III) was calculated from the difference in experimentally measured concentrations
258 of total dissolved iron and dissolved Fe(II).

259 Additionally, the dissolved Fe(III) could precipitate out as the pH increased, and
260 then the Fe mineralogy of the deposit was also observed. NAu-2 released about
261 300 μM of dissolved Fe at pH 2. The dissolving solution (200 mL) was sampled
262 after filtration (0.2 μm polycarbonate filter). The clear solution was subjected to
263 changing acidity from pH 2 to 5 by the stepwise addition of dilute NH₄OH. The
264 precipitated particles were separated out by 0.2 μm filters and were used in TEM
265 and Mössbauer analysis. Size distributions for the Fe-bearing particles formed in
266 the suspensions were determined by a Horiba LB-500 light scattering microscopy
267 within the size range of 3-6000 nm.

268 **3 Results and discussion**

269 **3.1 Characterization of mineral samples**

270 The characteristic results are shown in Table S1 and Table S2. The samples
271 exhibited S_{BET} in the range from 4.3 ± 0.3 to 22.6 ± 2.3 m²/g. The Fe_T content were
272 $5.45 \pm 0.34\%$, $26.30 \pm 0.57\%$, $2.36 \pm 0.56\%$ and $1.48 \pm 0.56\%$, for IMt-2, NAu-2,



273 SWy-2 and ATD, respectively. The proportions of Fe₂O₃ in IMt-2, NAu-2, SWy-2
274 and ATD were 7.95%, 39.03%, 5.55% and 2.57%, respectively.

275 **3.2 Effect of simulated CP on heterogeneous transformation of SO₂**

276 The *in situ* DRIFTS spectra on the IMt-2, NAu-2, SWy-2 and ATD samples before
277 and after CP exposed to SO₂ as a function of time are shown in Figure 1. For the
278 IMt-2 sample before CP (Figure 1a and 1b), the intensities of the broad peaks from
279 3600 to 3000 cm⁻¹ and a weak peak at 1650 cm⁻¹ increased with time. The band
280 between 3600 and 3000 cm⁻¹ was attributed to the vibrations of hydrogen-bonded
281 hydroxyl species (Zhao et al., 2015), while the absorption peak at 1650 cm⁻¹ was
282 mainly associated to H₂O produced from the reaction between SO₂ and surface
283 hydroxyls (Nanayakkara et al., 2012; Cheng et al., 2016). A weak vibration was
284 observed at around 1100 cm⁻¹, which might be attributed to free sulfate anions on the
285 particle surface (Ullerstam et al., 2003; Nanayakkara et al., 2012; Yang et al., 2016).
286 Previous studies established that various types of surface OH groups are the key
287 reactive sites for sulfite/sulfate and bisulfite/bisulfate formation on mineral oxides
288 (Faust et al., 1989; Usher et al., 2003; Ullerstam et al., 2003), because of the
289 complexes formed between sulfite/sulfate species and the surface OH. Generally, the
290 SO₂ adsorption grow in intensity with decreasing OH stretching and H₂O banding
291 (Zhang et al., 2006). However, the OH peaks herein were not observed to decrease
292 with prolonged time, because the losses of H₂O and OH groups on the particle
293 surfaces were replenished by maintaining the constant RH in this study.

294 When the same set of experiments were carried out using the IMt-2 sample after CP
295 (Figure 1b), the intensities of the prominent peaks were significantly higher than those
296 on the IMt-2 sample before CP. Four new bands were readily observed at 1167, 1100,
297 1088 and 1077 cm⁻¹. The new bands were easily assigned to the stretching motion of



298 surface-coordinated sulfate species (1167 cm^{-1}), i.e., bidentate surface sulfate
299 complexes, free sulfate ion (1100 cm^{-1}), and sulfite/bisulfite species (1088 and 1077
300 cm^{-1}) (Peak et al., 1999; Ullerstam et al., 2003; Yang et al., 2016). These new bands
301 remained when an argon blow-off process was carried out, suggesting that the
302 surface-adsorbed sulfite/sulfate species between 1250 and 1000 cm^{-1} was
303 chemisorbed (Zhang et al., 2006).

304 Upon adsorption of SO_2 on the surface of the N Au-2 sample before CP (Figure 1c
305 and 1d), the broad band from 3600 to 2800 cm^{-1} and the peaks at 1580 and 1675 cm^{-1}
306 increased drastically with time. These absorbance bands were all attributed to the
307 surface hydroxyl species (OH) and H_2O . No peaks were observed over the range of
308 1000 to 1250 cm^{-1} , suggesting that the sulfite/sulfate products were not formed newly
309 on the surface of the N Au-2 sample before CP. Upon adsorption of SO_2 on the surface
310 of the N Au-2 sample after CP (Figure 1d), the new bands at 3661 and 3450 cm^{-1} , the
311 broad band between 3400 and 2700 cm^{-1} , and the broad band centered at 2131 cm^{-1} ,
312 were observed as the exposure time increased. In detail, the band at 3661 cm^{-1} could
313 be assigned to stretching vibration modes of isolated or bridged surface hydroxyl
314 groups bonded to the surface iron ions embedded in the octahedral and tetrahedral
315 sites (Faust et al., 1989; Nanayakkara et al., 2012; Zhao et al., 2015). The peaks at
316 around 3450 cm^{-1} , 2131 cm^{-1} and the band between 3400 and 2700 cm^{-1} were all
317 attributed to surface OH groups (Ma et al., 2010; Zhao et al., 2017). These new bands
318 generated on the processed N Au-2 particles suggested that CP changed the location of
319 diverse OH groups on the particle surfaces. Over the range of 1250 - 1000 cm^{-1} , the
320 new bands centered at 1170 cm^{-1} was assigned to the asymmetric stretching of sulfate
321 (Kong et al., 2014; Yang et al., 2015).



322 The spectra of the SWy-2 samples before and after CP (Figure 1e and f) showed a
323 similar spectral character with those of the NAu-2 samples. The spectra for the ATD
324 samples before and after CP (Figure 1g and h) were roughly the same as the ones for
325 IMt-2. All of the results demonstrated that the characteristic peaks for the active OH
326 sites and the sulfite/sulfate products on the mineral particles after CP were
327 significantly higher than those on the ones before CP, indicating the higher
328 hygroscopicity and more SO₂ uptake on the particles after CP. The data shown herein
329 confirmed that CP could potentially promote the transformation of SO₂ on the particle
330 surfaces.

331 **Figure 1**

332 **3.3 Uptake coefficient of SO₂ on the mineral particles before and after CP**

333 The areas of the bands (from 1250 to 1000 cm⁻¹) attributed to the sulfite/sulfate
334 products as a function of time are shown in Figure 2. It was evident that the peak
335 areas of the products on the mineral particles after CP were generally greater than the
336 ones before CP. The reaction on the sample surfaces was practically saturated to SO₂
337 uptake within 15 min, except for the NAu-2 and IMt-2 samples after CP. As for all of
338 the sample, the saturation coverages of the sulfite/sulfate products after CP were
339 obviously greater than the corresponding values before CP, suggesting that CP
340 favored the sulfate formation on the mineral surfaces due to improving active site
341 number, as expected previously.

342 **Figure 2**

343 The maximum uptake coefficients (γ_{geo} and γ_{BET}) for SO₂ uptake on the samples
344 were estimated on the basis of the sulfate formation rates in the initial 15 min. The
345 values on the mineral samples before and after CP are shown in Table 1. The γ_{geo}
346 values of SO₂ on the IMt-2, NAu-2, SWy-2 and ATD samples before CP were



347 1.03×10^{-7} , 0.30×10^{-7} , 1.72×10^{-7} and 1.37×10^{-7} , respectively, which were in the order
348 of SWy-2, ATD, IMt-2 and NAu-2. The γ_{geo} values of SO_2 on the IMt-2, NAu-2,
349 SWy-2 and ATD samples after CP were 4.7, 19.4, 2.7 and 2.0 times higher than the
350 values before CP, respectively, suggesting that the SO_2 uptake on the mineral particles
351 significantly increased after CP.

352 A_{BET} was more appropriate to represent the effective area, because the reactant may
353 diffuse into tiny holes of the entire sample. The γ_{BET} values of SO_2 on the IMt-2,
354 NAu-2, SWy-2 and ATD samples before CP were 2.62×10^{-12} , 0.75×10^{-12} , 3.70×10^{-12}
355 and 1.61×10^{-11} , respectively, which were in the order of ATD, SWy-2, IMt-2 and
356 NAu-2. It was noteworthy that the S_{BET} of samples increased after CP, as shown in
357 Table 1. The γ_{BET} values of SO_2 on the IMt-2, NAu-2, SWy-2 and ATD after CP were
358 2.2, 4.1, 1.5 and 1.4 times higher than the values before CP, respectively. The
359 discrepancies in the γ_{BET} value confirmed that the higher sulfate formation rates of the
360 particles after CP was not only due to the increased surface area of the particles, but
361 also resulting from the chemical modification on the particle surfaces.

362 The estimated uptake coefficients were several orders of magnitude lower than the
363 results from Ullerstam et al. (2003) and Usher et al. (2003), which could be partly
364 explained by the difference in the preparation of mineral dust samples, or the
365 difference between diverse experimental structures such as the DRIFTS and Knudsen
366 cell in kinetics discussion. In this study, mineral dust particles were in a highly
367 accumulative state in the sample support of Knudsen cell. The many layers of
368 particles in the latter study will hinder the diffusion of gas into the underlayer
369 particles, resulting in the underestimate of γ_{BET} . However, the values herein were
370 comparable to those obtained by the similar DRIFTS setup (Fu et al., 2007),
371 indicating the reliability of our measurements.



372 In addition, the formation rate of sulfate appeared a linear increasing trend as a
373 function of pH cycles. Specifically, the increasing amount of sulfate ions for the
374 IMt-2, N Au-2, SWy-2 and ATD samples after each pH cycle during CP were 7.0×10^{10} ,
375 1.0×10^{11} , 5.0×10^{10} , 3.0×10^{10} , in the order of N Au-2 > IMt-2 > SWy-2 > ATD (Figure
376 3). The γ_{BET} (γ_{geo}) for IMt-2, N Au-2, SWy-2 and ATD after CP were 2.2 (4.7), 4.1
377 (19.4), 1.5 (2.7) and 1.4 (2.0) times greater than the corresponding values for those
378 without CP procedure, respectively. The multiples factors for γ_{BET} (γ_{geo}) were
379 coincided with the total Fe content of these samples: N Au-2 (26.30%) > IMt-2
380 (5.45%) > SWy-2 (2.36%) > ATD (1.48%). We thus supposed that the SO₂ uptake on
381 these dust samples were closely related to the Fe hosted in the particles.

382 **Figure 3**

383 3.4 Morphological change of the mineral particles after CP.

384 Figure 4 shows the TEM images of the mineral particles before and after CP. As
385 shown in Figure 4 a, c, e and g, the IMt-2, N Au-2, SWy-2 and ATD samples before
386 CP primarily consisted of laminar aluminosilicate with irregular shape and rough
387 morphologies mainly at the micrometer scale, all of which were characterized by
388 various fractions of Fe (1.5%-26.2%), along with minor Mg (0.1%-16.5%), K
389 (0.0%-7.8%) and Ca (0.0%-1.1%). The Fe within the aluminosilicates of the particles
390 was evenly distributed. Besides, some Fe-rich crystal with several hundreds of
391 nanometers in size were found to attach onto the ATD particles, which were identified
392 as α -Fe₂O₃ (PDF: 33-664) from the typical *d*-spacing analysis of HRTEM (Janney et
393 al., 2000).

394 After the simulated CP, all of the processed mineral particles showed much smaller
395 size than the ones before CP. For example, the typical IMt-2 and N Au-2 particles after
396 CP (Figure 4 b and d) were < 1 μm in size. Under the TEM, the average Fe content of



397 the individual IMt-2 and SWy-2 particles (Figure 4 b and f) decreased from 5.5% (\pm
398 1.9%; $n = 50$) to 4.1% ($\pm 1.6%$; $n = 50$) and from 2.4% ($\pm 0.6%$; $n = 50$) to 2.1% (\pm
399 0.5%; $n = 50$), respectively. In addition, the IMt-2 particles after CP showed a
400 heterogeneous distribution of the Fe on the basis of the EDX data. Most of the
401 aluminosilicate in IMt-2 after CP hosted lower Fe content (4.1%), whereas a few of
402 the Fe-rich particles with less Si/Al were observed with irregular shapes at the
403 nanoscale. The TEM images of the NAu-2 and ATD particles after CP (Figure 4 h)
404 showed some pseudo-hexagonal nanoparticles with around 5 nm in diameter. Based on
405 the EDX and SAED analysis, these nanoparticles were Fe-rich and the d -spacings was
406 at about 1.5-2.5 Å, all of which were identified to be 2-line ferrihydrite (Janney et al.,
407 2000; Shi et al., 2009).

408 The TEM observation suggested that CP induced the disintegration of mineral
409 particles and thus produced enhanced surface area, resulting in more active sites
410 available on the particle surfaces for SO₂ uptake. Results of TEM also showed that CP
411 influenced the Fe mineralogy, and lead to the Fe-rich nanoparticle formation, which
412 could partly explain the higher SO₂ uptake on the mineral particles after CP.

413 **Figure 4**

414 **3.5 Fe speciation analysis before and after CP.**

415 The fractions of “free-Fe” (including Fe_A and Fe_D) and “structural-Fe” in the
416 mineral particles before and after CP were determined by the CBD extraction (Figure
417 5). In terms of total Fe, the amorphous Fe (Fe_A) (e.g., nanoparticulate and poorly
418 crystalline ferrihydrite) contents of the IMt-2, NAu-2, SWy-2 and ATD samples
419 before CP were 0.7%, 0.5%, 0.7% and 3.8%, respectively. The crystalline Fe
420 (oxyhydr)oxides (Fe_D) (e.g., α -FeOOH and α -Fe₂O₃) contents of the IMt-2, NAu-2,
421 SWy-2 and ATD samples before CP were 7.2%, 2.3%, 4.5% and 35.5%, respectively.



422 As a result, the fractions of “structural-Fe” before CP were 92.1%, 97.2%, 94.8% and
423 60.7%, respectively, for IMt-2, NAu-2, SWy-2 and ATD.

424 After CP, the Fe_A contents of the IMt-2, NAu-2, SWy-2 and ATD samples reached
425 1.8%, 1.2%, 1.7% and 24.2%, respectively, which increased by 2.6, 2.4, 2.4 and 6.4
426 times as compared to the ones before CP. The crystalline Fe (oxyhydr)oxides (Fe_D)
427 contents of the samples after CP were not significantly changed as compared to the
428 ones before CP; whereas the content of “structural-Fe” in the Al-Si crystals of the
429 IMt-2, NAu-2, SWy-2 and ATD samples after CP decreased by various degrees, to
430 91.1%, 96.1%, 93.2% and 42.5%, respectively. We thus proposed that the increased
431 fractions of Fe_A could be mostly transformed from the “structural-Fe” in the
432 aluminosilicate phase of the particles during CP, which is in good agreement with the
433 TEM observation. For example, the Fe_A in the ATD samples increased from 3.8% to
434 24.2% after CP, accompanied by a sharp decrease of the structural-Fe content from
435 60.7% to 42.5%.

436 **Figure 5**

437 The Mössbauer spectra and their fitted results are shown in Figure 6. The
438 corresponding hyperfine parameters estimated from the best fitted spectra are
439 presented in Table S3. The central doublet with isomer shift (IS) of 0.37 mm s^{-1} and
440 quadrupole shift (QS) of 0.72 mm s^{-1} were typical for high-spin Fe(III) in octahedral
441 symmetry (Eyre and Dickson, 1995), while the other one with IS of 1.12 mm s^{-1} and
442 QS of 2.65 mm s^{-1} was characteristic of high spin Fe(II) (Hofstetter et al., 2003;
443 Kopcewicz et al., 2015). The two doublet components of the IMt-2, NAu-2, SWy-2
444 and ATD samples before CP were all attributed to different fractions of Fe(III) and
445 Fe(II) in the aluminosilicate crystals, respectively. Before CP, the Fe(II) fraction in the
446 IMt-2, NAu-2, SWy-2 and ATD samples were 34.0 %, 12.9 %, 18.3 % and 29.0 %, respectively.



447 respectively (Figure 6 a, c, e and g). Furthermore, the spectra of the ATD sample
448 before CP showed not only two central quadrupole doublets, but also one MHS sextet
449 with IS of 0.39 mm s^{-1} , QS of -0.13 mm s^{-1} and H_f of 51.1 T. The MHS sextet, which
450 shared 31.8 % of the whole area, could be ascribed to $\alpha\text{-Fe}_2\text{O}_3$ (Kopcewicz and
451 Kopcewicz et al., 1991), in agreement with the TEM analysis and “free-Fe”
452 measurement as mentioned previously.

453 After CP, the Fe(II) content of the samples decreased to 31.5 %, 11.6 %, 17.1% and
454 10.9%, respectively, for IMt-2, NAu-2, SWy-2 and ATD (Figure 6 b, d, f and h). It
455 was supposed that the Fe(II) release is more energetically favorable than one of Fe(III)
456 due to the bond strength. As to the ATD sample after CP (Figure 6 h), not only did the
457 Fe(II) fraction decrease from 29.0% to 10.9%, but also the Fe(III) fraction in the
458 aluminosilicates decreased from 39.0% to 33.0%. Meanwhile, the $\alpha\text{-Fe}_2\text{O}_3$ fraction
459 was not significantly changed (31.8% vs. 32.3%). As discussed previously, the Fe
460 mobilization was dependent on the specific chemical bonds. The Fe_D phase in
461 $\alpha\text{-Fe}_2\text{O}_3$ with the strong Fe–O bond was less liable than that embedded in the
462 aluminosilicate lattice (Strehlau et al., 2017). It was well documented that the Fe
463 replacing alkaline elements as the interlayer ions was easy to be mobilized than the Fe
464 bound by covalent bonds in the aluminosilicate matrix (Luo et al., 2005; Cwiertny et
465 al., 2008; Journet et al., 2008). Therefore, the Fe in the aluminosilicate fraction of the
466 mineral particles exhibited varied iron solubility.

467 Particularly, a new quadrupole doublet with IS of 0.67 mm s^{-1} and QS of 1.21 mm
468 s^{-1} was observed in the spectra of the ATD sample after CP (Figure 6 h), which shared
469 23.8% of the total area, and was possibly indicative of the Fe(III) oxide hybridized in
470 the aluminosilicate matrix (Kopcewicz and Kopcewicz, 1991). The “free-Fe”
471 measurement have indicated that the Fe_A fraction of ATD increased by 20.4% after CP,



472 so that this Fe phase was most likely to be amorphous Fe(III) hybridized with Al/Si.
473 In the terms of the other samples after CP, the magnetic signal of the newly formed
474 Fe(III) phase was not detected. It was probably due to the newly formed Fe fractions
475 were not available at sufficiently high level to be clearly resolved by the Mössbauer
476 spectroscopy, and/or the slight signal drift and the poor signal to noise ratio made an
477 unambiguous identification difficult. Herein, the newly formed amorphous Fe(III)
478 phase was supposed to be a reactive Fe-bearing component, of which may contribute
479 significantly to the SO₂ uptake even at a low level.

480 **Figure 6**

481 **3.6 The dissolution-precipitation cycle of the mineral Fe during CP**

482 During the simulated CP experiments, the concentrations of total dissolved Fe (Fe_s),
483 dissolved Fe(II) and Fe(III) released from the particles as a function of time are shown
484 in Figure 7. Similar dissolution trends were observed for all of the samples. One can
485 see that the suspensions at pH 2 induced a rapid increase of Fe_s. Once increasing the
486 pH from 2 to 5 resulted in a rapid and almost complete removal of Fe_s. In fact, only a
487 rather small fraction of the Fe in dusts could be dissolved at pH above 4 (Zuo and
488 Hoigne, 1992). The dissolved Fe precipitated rapidly as insoluble deposit at pH 5.
489 When the suspension pH was again reduced to 2, a steep increase in the Fe_s
490 concentration was measured once again. The fast Fe release was due to the
491 redissolution of the Fe-rich precipitates, which was proposed to be reactive Fe phases.
492 Such highly soluble Fe-bearing precipitates have been observed under the TEM, as
493 well as the “free Fe” measurement and Mössbauer characterization.

494 **Figure 7**

495 For each pH cycle during the simulated CP experiment, the overall changes of total
496 released Fe concentrations were reproducible. The Fe ion on the particle surfaces



497 would experience a continuous dissolution-precipitation-redissolution-reprecipitation
498 process when the pH cycles between pH 2 and pH 5 (cloud-aerosol modes). During
499 this process, the Fe(II) fraction would be transformed to Fe(III). The results shown
500 herein suggested that CP could significantly modify Fe partitioning between dissolved
501 and particulate phases in the real atmosphere. Not only did the increase of specific
502 surface area contribute to the enhanced sulfate formation, but also the highly reactive
503 Fe on the particle surfaces yielded during CP were also responsible for the higher SO₂
504 uptake on the particles after CP.

505 When investigating the NAu-2 sample, once the pH of the clear solution increased
506 from 2 to 5-6, the Fe-bearing nanoparticles separated out from the solution rapidly
507 and precipitate out slowly. It developed an initial yellow color and then an orange
508 colored suspension. The TEM images of the precipitated particles are shown in Figure
509 8. The particles could be categorized into two different types. One type of particle
510 could be characterized as hundreds of nanometers in size, with low Fe but high Si/Al
511 content. The other type displayed particle sizes nearly 1 micrometer, and were Fe-rich
512 but contained a smaller amount of Si/Al components. These bigger particles were
513 ambiguously identified as Na_{0.42}Fe₃Al₆B₃₀₉Si₆O₁₈(OH)_{3.65} (PDF: 89-6506) on the
514 basis of the EDX data and SAED analysis. It is likely that the Al/Si elements also
515 precipitated out along with the Fe.

516 **Figure 8**

517 The Mössbauer spectra of the precipitated Fe-rich particles are shown in Figure 9.
518 Two central doublets were distinguished, with one (48.4%) of IS = 0.45 mm s⁻¹, QS =
519 0.75 mm s⁻¹, and the other (51.6%) of IS = 0.24 mm s⁻¹, QS = 0.76 mm s⁻¹. Both of
520 the two doublet components could be attributed to the Fe(III) fraction in the
521 aluminosilicates (Kopcewicz et al., 2015). The results were in good agreement with



522 the TEM observation, which showed that most of these Fe particles were mostly
523 present as the Fe(III) hybridized with Al/Si. The particle size distributions in the
524 suspensions were also determined by dynamic light scattering, as shown in Figure 10.
525 When pH was lower than 2.0, the particles seemed to stabilize below 10 nm in size.
526 These Fe colloids were thought to be a source of soluble Fe (Janney et al., 2000).
527 Once pH increased, the size of precipitated particles quickly increased, even to
528 micro-scale, and the suspension was featured with a polydispersed size distribution.

529 Conclusively, the precipitated Fe were mainly Fe(III) with weak crystal structure
530 and/or ferrihydrite nanoparticle hybridized with Al/Si, which were possibly
531 transformed from the Fe hosted in the aluminosilicate matrix of the particles. The
532 particle surfaces after CP was coated by these reactive Fe, resulting in enhanced SO₂
533 uptake.

534 **Figure 9**

535 **Figure 10**

536 **4 Conclusion and implication**

537 Transition metal ions, especially Fe(III), could catalyze SO₂ oxidation rapidly in
538 cloud drops (Harris et al., 2013). This study further confirmed that SO₂ uptake on the
539 mineral particles could be greatly enhanced during CP, possibly more than described
540 previously. The higher uptake coefficient of the particles after CP was not only due to
541 increased surface area, but also resulted from the chemical modification of the particle
542 surfaces. The “free-Fe” and Mössbauer analysis suggested that CP triggered newly
543 formation of amorphous Fe particles on the surfaces, of which were mostly
544 transformed from the Fe hosted in the aluminosilicate matrix. TEM showed that the
545 amorphous Fe(III) and/or ferrihydrite nanoparticle were hybridized with Al/Si. In
546 general, the acidity fluctuation during CP enables the dissolution-precipitation cycles



547 of mineral Fe to yielded more reactive Fe, resulting in more SO₂ uptake on the
548 particle surfaces. More SO₂ adsorption further increases the surface acidity of dust
549 particles, in turn leading to higher Fe solubility; again, more sulfate formation. It was
550 thus proposed that there is a positive feedback relative to SO₂ uptake and iron
551 mobilized from mineral particles during CP, therefore enhanced sulfate formation
552 greatly.

553 Our results also serve to explain high sulfate loading in fog-haze episodes of China.
554 It has been recommended that sulfate contributed significantly to the explosive
555 growth of fine particles, thus exacerbating severe fog-haze development (Kasibhatla
556 et al., 1997; Nie et al., 2014; Barrie et al., 2016). Haze and fog within an episode was
557 often found to transform each other at a short time due to the diurnal variation of RH,
558 whereby the haze-fog transition was probably analogous to the aerosol-cloud
559 interaction. Water content of aerosol or fog drops was regulated by RH, and thus
560 allowed the particle acidity fluctuation. Although the aerosol acidity could not be
561 accurately determined from field measurements or calculated using the
562 thermodynamic model, we recognized that the large pH fluctuations between the
563 haze-fog modes could significantly modify the microphysical properties of mineral
564 particles, and triggered formation of reactive Fe particles and thus accelerated sulfate
565 formation via a self-amplifying process, contributing to explosive growth of fine
566 particles at the initial stage of fog-haze events. The data presented herein also
567 highlight that CP provide more bioavailable iron from mineral particle than one
568 expected previously, of which is a key speciation to promote oceanic primary
569 productivity. Results of this study could partly explain the missing source of sulfate
570 and improve agreement between models and field observations.



571 Additionally, previous studies indicated that Fe in pyrogenic aerosols was always
572 presented as liable Fe, such as ferric sulfate and aggregated nanocrystals of magnetite
573 (Fe_3O_4) (Fu et al., 2012), and displayed higher Fe solubility compared to dust
574 (Desboeufs et al., 2005; Sedwick et al., 2007; Ito et al., 2019). Alexander et al.
575 demonstrated that the sulfate formed through metal catalysis was highest over the
576 polluted industrial regions of northern Eurasia, suggesting that the increasing
577 importance of the metal-catalyzed S(IV) oxidation pathway due to anthropogenic
578 emissions (Alexander et al, 2009). With the rapid development of industry and
579 agriculture, the pyrogenic Fe-containing aerosols are indispensable contributors to the
580 atmospheric Fe load in China. Thus, the acidic solution at pH 2 and high sulfate
581 loading of fine particles in severe fog-haze events of China might be more relevant to
582 Fe-containing combustion aerosols than mineral dust. Based on the current findings,
583 not only the potential influences of cloud liquid water content, light, and organic
584 ligands, but also the solubility and speciation of Fe in pyrogenic aerosols will be
585 considered during the simulated CP experiments in the future. A more detailed
586 understanding of the iron-sulfur cycle during CP is therefore critical to estimate
587 accurately the contribution of CP to global sulfate loading and its impact on the
588 climate.

Author contributions. Z.W., H.F. and J.C. designed the experiments, Z.W., T.W., H.F.
and L.Z. performed the laboratory experiments. H.F., J.C., L.Z. and V.G. contributed
reagents/analytic tools. C.G., V.G. and M.T. gave some valuable suggestions in



designing the experiments. Z.W., T.W. and H.F. analyzed data. Z.W. and H.F. wrote the manuscript, with inputs from all coauthors.

Competing interests. The authors declare no conflict of interest.

Acknowledgments. This work was supported by National Key R&D Program of China (2016YFC0202700), National Natural Science Foundation of China (Nos. 91744205, 21777025, 21577022, 21177026), and International Cooperation Project of Shanghai Municipal Government (15520711200) and Opening Project of Shanghai Key Laboratory of Atmospheric Particle Pollution and Prevention.

References

- Alexander, B., Park, R. J., Jacob, D. J., and Gong, S.: Transition metal-catalyzed oxidation of atmospheric sulfur: Global implications for the sulfur budget, *J. Geophys. Res.*, 114, D02309, 2009.
- Andreae, M. O., and Rosenfeld, D.: Aerosol-cloud-precipitation interactions. Part 1. The nature and sources of cloud-active aerosols, *Earth Sci. Rev.*, 89, 13-41, 2008.
- Baker, A. R., and Croot, P. L.: Atmospheric and marine controls on aerosol iron solubility in seawater, *Mar. Chem.*, 120, 4-13, 2010.
- Barrie, L. A., Yi, Y., Leitch, W. R., Lohmann, U., Kasibhatla, P., Roelofs, G. J., Wilson, J., McGovern, F., Benkovitz, C., Mélières, M. A., Law, K., Prospero, J., Kritz, M., Bergmann, D., Bridgeman, C., Chin, M., Christensen, J., Easter, R., Feichter, J., Land, C., Jeuken, A., Kjellström, E., Koch, D., and Rasch, P.: A comparison of large-scale atmospheric sulphate aerosol models (COSAM): Overview and highlights, *Tellus B*, 53, 615-645, 2016.
- Behra, P., Sigg, L., and Stumm, W.: Dominating influence of NH_3 on the oxidation of aqueous



- SO₂: the coupling of NH₃ and SO₂ in atmospheric water, *Atmos. Environ.*, 23, 2691-2707, 1989.
- Cheng, Y. F., Zheng, G. J., Wei, C., Mu, Q., Zheng, B., Wang, Z. B., Gao, M., Zhang, Q., He, K. B., Carmichael, G., Poschl, U., and Su, H.: Reactive nitrogen chemistry in aerosol water as a source of sulfate during haze events in China, *Sci. Adv.*, 2, 1-11, 2016.
- Claquin, T., Schulz, M., and Balkanski, Y. J.: Modeling the mineralogy of atmospheric dust sources, *J. Geophys. Res.-Atmos.*, 104, 22243-22256, 1999.
- Cwiertny, D. M., Baltrusaitis, J., Hunter, G. J., Laskin, A., Scherer, M. M., and Grassian, V. H.: Characterization and acid-mobilization study of iron-containing mineral dust source materials, *J. Geophys. Res.-Atmos.*, 113, D05202, 2008.
- Deguillaume, L., Desboeufs, K. V., Leriche, M., Long, Y., and Chaumerliac, N.: Effect of iron dissolution on cloud chemistry: from laboratory measurements to model results, *Atmos. Pollut. Res.*, 1, 220-228, 2010.
- Desboeufs, K. V., Losno, R., and Colin, J. L.: Factors influencing aerosol solubility during cloud processes, *Atmos. Environ.*, 35, 3529-3537, 2001.
- Desboeufs, K. V., Sofikitis, A., Losno, R., Colin, J. L., and Auset, P.: Dissolution and solubility of trace metals from natural and anthropogenic aerosol particulate matter, *Chemosphere*, 58, 195-203, 2005.
- Eyre, J. K., and Dickson, D. P. E.: Mössbauer spectroscopy analysis of iron-containing minerals in the Chinese loess, *J. Geophys. Res.*, 100, 17925-17930, 1995.
- Faust, B. C., Hoffmann, M. R., and Bahnemann, D. W.: Photocatalytic oxidation of sulfur dioxide



- in aqueous suspensions of α -Fe₂O₃, *J. Phys. Chem.*, 93, 6371-6381, 1989.
- Fu, H. B., Wang, X., Wu, H. B., Yin, Y., and Chen, J. M.: Heterogeneous uptake and oxidation of SO₂ on iron oxides, *J. Phys. Chem. C*, 111, 6077-6085, 2007.
- Fu, H. B., Lin, J., Shang, G. F., Dong, W. B., Grassian, V. H., Carmichael, G. R., Li, Y., and Chen, J. M.: Solubility of iron from combustion source particles in acidic media linked to iron speciation, *Environ. Sci. Technol.*, 46, 11119-11127, 2012.
- Formenti, P., Rajot, J. L., Desboeufs, K., Caquineau, S., Chevaillier, S., Nava, S., Gaudichet, A., Journet, E., Triquet, S., Alfaro, S., Chiari, M., Haywood, J., Coe, H., and Highwood, E.: Regional variability of the composition of mineral dust from western Africa: Results from the AMMA SOP0/DABEX and DODO field campaigns, *J. Geophys. Res.*, 113, D00C13, 2008.
- George, C., Ammann, M., D'Anna, B., Donaldson D. J., and Nizkorodov, S. A.: Heterogeneous Photochemistry in the Atmosphere, *Chem. Rev.*, 115, 4218-4258, 2015.
- Goodman, A. L., Li, P., Usher, C. R., and Grassian, V. H.: Heterogeneous uptake of sulfur dioxide on aluminum and magnesium oxide particles, *J. Phys. Chem. A*, 105, 6109-6120, 2001.
- Harris, E., Sinha, B., Foley, S., Crowley, J. N., Borrmann, S., and Hoppe, P.: Sulfur isotope fractionation during heterogeneous oxidation of SO₂ on mineral dust, *Atmos. Chem. Phys.*, 12, 4867-4884, 2012.
- Harris, E., Sinha, B., van Pinxteren, D., Tilgner, A., Fomba, K. W., Schneider, J., Roth, A., Gnauk, T., Fahlbusch, B., Mertes, S., Lee, T., Collett, J., Foley, S., Borrmann, S., Hoppe, P.,



- and Herrmann, H.: Enhanced role of transition metal ion catalysis during in-cloud oxidation of SO₂, *Science*, 340, 727-730, 2013.
- Herman, L. M. S.: Heterogeneous and homogeneous oxidation of SO₂ in the remote marine atmosphere, *Atmos. Environ.*, 25, 1489-1496, 1991.
- Huang, L., Zhao, Y., Li, H., and Chen, Z.: Kinetics of heterogeneous reaction of sulfur dioxide on authentic mineral dust: Effects of relative humidity and hydrogen peroxide, *Environ. Sci. Technol.*, 49, 10797-17805, 2015.
- Hofstetter, T. B., Schwarzenbach, R. P., and Haderlein, S. B.: Reactivity of Fe(II) species associated with clay minerals, *Environ. Sci. Technol.*, 37, 519-528, 2003.
- Ito, A., Myriokefalitakis, S., Kanakidou, M., Mahowald, N., Scanza, R., Hamilton, D., Baker, A., Jickells, T., Sarin, M., Bikkina, S., Gao, Y., Shelley, R., Buck, C., Landing, W., Bowie, A., Perron, M., Guieu, C., Meskhidze, N., Johnson, M., Feng, Y., Kok, J., Nenes, A. and Duce, R.: Pyrogenic iron: The missing link to high iron solubility in aerosols, *Sci. Adv.*, 5(5), eaau7671, 2019.
- Janney, D. E., Cowley, J. M., and Buseck, P. R.: Transmission electron microscopy of synthetic 2- and 6-line ferrihydrite, *Clay Clay Miner.*, 48, 111-119, 2000.
- Jickells, T. D., An, Z. S., Andersen, K. K., Baker, A. R., Bergametti, G., Brooks, N., Cao, J. J., Boyd, P. W., Duce, R. A., Hunter, K. A., Kawahata, H., Kubilay, N., laRoche, J., Liss, P. S., Mahowald, N., Prospero, J. M., Ridgwell, A. J., Tegen, I., and Torres, R.: Global iron connections between desert dust, ocean biogeochemistry, and climate, *Science*, 308, 67-71, 2005.



- Journet, E., Desboeufs, K. V., Caquineau, S., and Colin, J.-L.: Mineralogy as a critical factor of dust iron solubility, *Geophys. Res. Lett.*, 35, L07805, 2008.
- Kadar, E., Fisher, A., Stolpe, B., Calabrese, S., Lead, J., Valsami-Jones, E., and Shi, Z.: Colloidal stability of nanoparticles derived from simulated cloud-processed mineral dusts, *Sci. Total. Environ.*, 466-467, 864-870, 2014.
- Kasibhatla, P., Chameides, W. L., and John, J. S.: A three-dimensional global model investigation of seasonal variations in the atmospheric burden of anthropogenic sulfate aerosols, *J. Geophys. Res.-Atmos.*, 102, 3737-3759, 1997.
- Kerminen, V. M., Pirjola, L., Boy, M., Eskola, A., Teinila, K., Laakso, L., Asmi, A., Hienola, J., Lauri, A., Vainio, V., Lehtinen, K., and Kulmala, M.: Interaction between SO₂ and submicron atmospheric particles, *Atmos. Res.*, 54, 41-57, 2000.
- Kolb, C. E., Cox, R. A., Abbatt, J. P. D., Ammann, M., Davis, E. J., Donaldson, D. J., Garrett, B. C., George, C., Griffiths, P. T., Hanson, D. R., Kulmala, M., McFiggans, G., Pöschl, U., Riipinen, I., Rossi, M. J., Rudich, Y., Wagner, P. E., Winkler, P. M., Worsnop, D. R., and O'Dowd, C. D.: An overview of current issues in the uptake of atmospheric trace gases by aerosols and clouds, *Atmos. Chem. Phys.*, 10, 10561-10605, 2010.
- Kong, L. D., Zhao, X., Sun, Z. Y., Yang, Y. W., Fu, H. B., Zhang, S. C., Cheng, T. T., Yang, X., Wang, L., and Chen, J. M.: The effects of nitrate on the heterogeneous uptake of sulfur dioxide on hematite, *Atmos. Chem. Phys.*, 14, 9451-9467, 2014.
- Kopcewicz, B., and Kopcewicz, M.: Mössbauer study of iron-containing atmospheric aerosols, *Struct. Chem.*, 2, 303-312, 1991.



- Kopcewicz, B., Kopcewicz, M., and Pietruczuk, A.: The Mössbauer study of atmospheric iron-containing aerosol in the coarse and PM_{2.5} fractions measured in rural site, *Chemosphere*, 131, 9-16, 2015.
- Lafon, S., Rajot, J.-L., Alfaro, S. C., and Gaudichet, A.: Quantification of iron oxides in desert aerosol, *Atmos. Environ.*, 38, 1211-1218, 2004.
- Lelieveld, J., and Heintzenberg, J.: Sulfate cooling effect on climate through in-cloud oxidation of anthropogenic SO₂, *Science*, 258, 117-120, 1992.
- Luo, C., Mahowald, N. M., Meskhidze, N., Chen, Y., Siefert, R. L., Baker, A. R., and Johansen, A. M.: Estimation of iron solubility from observations and a global aerosol model, *J. Geophys. Res.*, 110, D23, 2005.
- Luo, C., Mahowald, N., Bond, T., Chuang, P. Y., Artaxo, P., Siefert, R., Chen, Y., and Schauer, J.: Combustion iron distribution and deposition, *Global Biogeochem. Cycles*, 22, GB1012, 2008.
- Luria, M., and Sievering, H.: Heterogeneous and homogeneous oxidation of SO₂ in the remote marine atmosphere, *Atmos. Environ.*, 25, 1489-1496, 1991.
- Ma, Q., He, H., and Liu, Y.: In situ DRIFTS study of hygroscopic behavior of mineral aerosol, *J. Environ. Sci.*, 22, 555-560, 2010.
- Mackie, D. S.: Simulating the cloud processing of iron in Australian dust: pH and dust concentration, *Geophys. Res. Lett.*, 32, L06809, 2005.
- Mahowald, N. M., Baker, A. R., Bergametti, G., Brooks, N., Duce, R. A., Jickells, T. D., Kubilay, N., Prospero, J. M., and Tegen, I.: Atmospheric global dust cycle and iron inputs



- to the ocean. *Global Biogeochem. Cycles*, 19, GB4025, 2005.
- Maters, E. C., Delmelle, P., and Bonneville, S.: Atmospheric processing of volcanic glass: Effects on iron solubility and redox speciation. *Environ. Sci. Technol.*, 50 (10), 5033-5040, 2016.
- Meskhidze, N.: Iron mobilization in mineral dust: Can anthropogenic SO₂ emissions affect ocean productivity? *Geophys. Res. Lett.*, 30, 1-2, 2003.
- Nanayakkara, C. E., Pettibone, J., and Grassian, V. H.: Sulfur dioxide adsorption and photooxidation on isotopically-labeled titanium dioxide nanoparticle surfaces: Roles of surface hydroxyl groups and adsorbed water in the formation and stability of adsorbed sulfite and sulfate, *Phys. Chem. Chem. Phys.*, 14, 6957-6966, 2012.
- Nie, W., Ding, A. J., Wang, T., Kerminen, V., George, C., Xue, L. K., Wang, W. X., Zhang, Q. Z., Petäjä, T., Qi, X. M., Gao, X. M., Wang, X. F., Yang, X. Q., Fu, C. B., and Kulmala, M.: Polluted dust promotes new particle formation and growth, *Sci. rep.*, 4, 6634, 2014.
- Peak, D., Ford, R. G., and Sparks, D. L.: An in situ ATR-FTIR investigation of sulfate bonding mechanisms on goethite, *J. Colloid Interface Sci.*, 218, 289-299, 1999.
- Pruppacher, H. R., Jaenicke, R.: The processing of water-vapor and aerosols by atmospheric clouds, a global estimate, *Atmos. Res.*, 38, 283-295, 1995.
- Rubasinghege, G., Lentz, R. W., Scherer, M. M., and Grassian, V. H.: Simulated atmospheric processing of iron oxyhydroxide minerals at low pH: roles of particle size and acid anion in iron dissolution, *Proc. Natl. Acad. Sci. U. S. A.*, 107, 6628-6633, 2010.
- Sedwick, P. N., Sholkovitz, E. R., and Church, T. M.: Impact of anthropogenic combustion



- emissions on the fractional solubility of aerosol iron: Evidence from the Sargasso Sea, *Geochem. Geophys. Geosyst.*, 8, Q10Q06, 2007.
- Shi, Z., Bonneville, S., Krom, M. D., Carslaw, K. S., Jickells, T. D., Baker, A. R., and Benning, L. G.: Iron dissolution kinetics of mineral dust at low pH during simulated atmospheric processing, *Atmos. Chem. Phys.*, 11, 995-1007, 2011.
- Shi, Z., Krom, M. D., Bonneville, S., Baker, A. R., Jickells, T. D., and Benning, L. G.: Formation of iron nanoparticles and increase in iron reactivity in mineral dust during simulated cloud processing, *Environ. Sci. Technol.*, 43, 6592-6596, 2009.
- Shi, Z., Krom, M. D., Bonneville, S., Baker, A. R., Bristow, C., Drake, N., Mann, G., Carslaw, K., McQuaid, J. B., Jickells, T., and Benning, L. G.: Influence of chemical weathering and aging of iron oxides on the potential iron solubility of Saharan dust during simulated atmospheric processing, *Global Biogeochem. Cycles*, 25, GB2010, 2011.
- Shi, Z., Krom, M. D., Bonneville, S., and Benning, L. G.: Atmospheric processing outside clouds increases soluble iron in mineral dust, *Environ. Sci. Technol.*, 49, 1472-1477, 2015.
- Siefert, R. L., Johansen, A. M., Hoffmann, M. R., and Pehkonen, S. O.: Measurements of trace metal (Fe, Cu, Mn, Cr) oxidation states in fog and stratus clouds, *J. Air Waste Manage.*, 48(2), 128-143, 1998.
- Spokes, L. J., Jickells, T. D., and Lim, B.: Solubilization of aerosol trace-metals by cloud processing - a laboratory study, *Geochim. Cosmochim. Acta.*, 58, 3281-3287, 1994.
- Strehlau, J. H., Schultz, J. D., Vindedahl, A. M., Arnold, W. A., and Penn, R. L.: Effect of nonreactive kaolinite on 4-chloronitrobenzene reduction by Fe(II) in goethite-kaolinite



- heterogeneous suspensions, *Environ. Sci.: Nano*, 4, 325-334, 2017.
- Sun, Y. L., Jiang, Q., Wang, Z. F., Fu, P. Q., Li, J., Yang, T., and Yin, Y.: Investigation of the sources and evolution processes of severe haze pollution in Beijing in January 2013, *J. Geophys. Res.-Atmos.*, 119, 4380-4398, 2014.
- Ullerstam, M., Johnson, M. S., Vogt, R., and Ljungstrom, E.: DRIFTS and Knudsen cell study of the heterogeneous reactivity of SO₂ and NO₂ on mineral dust, *Atmos. Chem. Phys.*, 3, 2043-2051, 2003.
- Usher, C. R., Al-Hosney, H., Carlos-Cuellar, S., and Grassian, V. H.: A laboratory study of the heterogeneous uptake and oxidation of sulfur dioxide on mineral dust particles, *J. Geophys. Res.-Atmos.*, 107, 161-169, 2002.
- Usher, C. R., Michel, A. E., and Grassian, V. H.: Reactions on mineral dust, *Chem. rev.*, 103, 4883-4940, 2003.
- Viollier, E., Inglett, P. W., Hunter, K., Roychoudhury, A. N., and Van Cappellen, P.: The ferrozine method revisited: Fe(II)/Fe(III) determination in natural waters, *Appl. Geochem.*, 15, 785-790, 2000.
- Wang, G., Wang, H., Yu, Y., Gao, S., Feng, J., Gao, S., and Wang, L.: Chemical characterization of water-soluble components of PM₁₀ and PM_{2.5} atmospheric aerosols in five locations of Nanjing, China, *Atmos. Environ.*, 37, 2893-2902, 2003.
- Wang, Y., Zhang, Q., Jiang, J., Zhou, W., Wang, B., He, K., Duan, F., Zhang, Q., Philip, S., and Xie, Y.: Enhanced sulfate formation during China's severe winter haze episode in January 2013 missing from current models, *J. Geophys. Res.-Atmos.*, 119, 10425-10440,



- 2014.
- Wu, L. Y., Tong, S. R., Wang, W. G., and Ge, M. F.: Effects of temperature on the heterogeneous oxidation of sulfur dioxide by ozone on calcium carbonate, *Atmos. Chem. Phys.*, 11, 6593-6605, 2011.
- Wurzler, S., Reisin, T. G., and Levin, Z.: Modification of mineral dust particles by cloud processing and subsequent effects on drop size distributions, *J. Geophys. Res.-Atmos.*, 105, 4501-4512, 2000.
- Yang, W., He, H., Ma, Q., Ma, J., Liu, Y., Liu, P., and Mu, Y.: Synergistic formation of sulfate and ammonium resulting from reaction between SO₂ and NH₃ on typical mineral dust, *Phys. Chem. Chem. Phys.*, 18, 956-964, 2016.
- Yang, W., Zhang, J., Ma, Q., Zhao, Y., Liu, Y., and He, H.: Heterogeneous reaction of SO₂ on manganese oxides: the effect of crystal structure and relative humidity, *Sci. rep.*, 7, 4550, 2017.
- Zhang, X., Zhuang, G., Chen, J., Wang, Y., Wang, X., An, Z., and Zhang, P.: Heterogeneous reactions of sulfur dioxide on typical mineral particles, *J. Phys. Chem. B*, 110, 12588-12596, 2006.
- Zhao, X., Kong, L., Sun, Z., Ding, X., Cheng, T., Yang, X., and Chen, J.: Interactions between heterogeneous uptake and adsorption of sulfur dioxide and acetaldehyde on hematite, *J. Phys. Chem. A*, 119, 4001-4008, 2015.
- Zhao, Y., Liu, Y., Ma, J., Ma, Q., and He, H.: Heterogeneous reaction of SO₂ with soot: The roles of relative humidity and surface composition of soot in surface sulfate formation,



Atmos. Environ., 152, 465-476, 2017.

Zhu, X., Prospero, J. M., Savoie, D. L., Millero, F. J., Zika, R. G., and Saltzman, E. S.:

Photoreduction of iron(III) in marine mineral aerosol solutions, *J. Geophys. Res.-Atmos.*,
98, 9039-9046, 1993.

Zhuang, G. S., Yi, Z., Duce, R. A., and Brown, P. R.: Link between iron and sulfur cycles

suggested by detection of Fe(II) in remote marine aerosols, *Nature*, 355 (6360), 537-539,
1992.

Zuo, Y. G., and Hoigne, J.: Formation of hydrogen-peroxide and depletion of oxalic-acid in

atmospheric water by photolysis of iron(III) oxalato complexes, *Environ. Sci. Technol.*, 26,
1014-1022, 1992.



Captions of Figures and Tables

Figure 1. Comparison of the DRIFT spectra of mineral dust samples upon exposure to SO₂ for 45 min before and after CP. Data for IMt-2 (a and b), NAu-2 (c and d), SWy-2 (e and f), ATD (g and h), are shown in the ranges of 4000 to 1250 cm⁻¹ and 1250 to 1000 cm⁻¹, respectively.

Figure 2. Comparison of the integrated areas on DRIFTS spectra in the range of 1250-1000 cm⁻¹ for the sulfate species formed on the samples before and after CP.

Table 1. Sulfate formation rates and uptake coefficients of SO₂ on particle samples before and after CP.

Figure 3. Comparison of the sulfate formation rates as a function of pH cycle.

Figure 4. Comparison of morphologies and chemical properties for samples collected before and after CP using TEM. The dotted circles indicate the positions of the electron beam for the HRTEM images and SAED patterns. Elements of the detected parts of individual particles are also presented. Square brackets indicate mass percent of iron. The iron species were identified by the Miller indices and the SAED patterns. (a) IMt-2 particles characterized by high fractions of Al and Si, along with other crustal elements including Mg, K and Fe. (b) IMt-2 particles after CP were almost all less than 1 μm in size. Some Fe-rich particles with less Si and Al were observed on nanoscale dimension. (c) NAu-2 particles with high Fe/Si-ratios, contain Mg, Al and Ca elements. (d) NAu-2 particles after CP were much smaller than the ones before CP. Some ferrihydrite clusters were observed and were attached on the surface of the NAu-2 particles after CP. (e) Typical SWy-2 particles were Al/Si-rich, containing Fe, Mg and Ca elements. (f) TEM images of the SWy-2 particles after CP appeared smaller than the particles before CP. (g) The Si/Al-rich crystal in ATD particles was



aluminosilicate with low content of Fe, and a typical of the α -Fe₂O₃ particles (PDF: 33-664) was found to attach onto the aluminosilicate surface. (h) The pseudo-hexagonal nanoparticles were observed to on the surface of α -Fe₂O₃ crystal among the ATD particles. The SAED lattice constant of these nanoparticles were found to be very close to that of 2-line ferrihydrite.

Figure 5. The fractions of “free-Fe” (Fe_A and Fe_B) and “structural-Fe” were measured by the chemical CBD extractions for the samples before and after CP. Results are present as relative percentage of Fe_T.

Figure 6. Mössbauer spectroscopy measured for samples. IMt-2 before and after CP (a and b), NAu-2 before and after CP (c and d), SWy-2 before and after CP (e and f), ATD before and after CP (g and h). Experimental data were fit using a least-squares fitting-program. The IS values were relative to α -Fe at RT. Prominent spectral features associated with different iron species are indicated.

Figure 7. The concentrations of Fe_s, dissolved Fe(II) and Fe(III) in the suspensions measured over 144 h in the solution cycled between pH 2 and pH 5 for IMt-2 (a), NAu-2 (b), SWy-2 (c) and ATD (d), respectively.

Figure 8. TEM images of the newly formed particles in the precipitation experiment. Based on the TEM-EDX measurement and SAED analysis, these particles could be categorized into two different types, which were circled in Figure 8 a. The typical sizes of the first type were hundreds of nanometers. The enlarged images are displayed in Figure 8 b, c and d. The insert EDX data and SAED image confirmed that they were poor crystalline aluminosilicate with low Fe but high Si/Al content. The second type (Figure 8 e, f and g) were Fe-rich but with less amount of Si/Al, which were nearly 1 micrometer in size. Based on the EDX data and the SAED



analysis, these bigger particles were ambiguously identified as $\text{Na}_{0.42}\text{Fe}_3\text{Al}_6\text{B}_{309}\text{Si}_6\text{O}_{18}(\text{OH})_{3.65}$ (PDF: 89-6506).

Figure 9. Mössbauer spectroscopy measured at RT for the neo-formed particles collected in the precipitation experiment.

Figure 10. During the precipitation experiment, the particle size distributions in the suspensions were determined by dynamic light scattering. The presented size distributions are characteristic of neo-formed nanoparticles or microparticles as the suspension pH raised from 1.0 to 3.8.



Figure 1

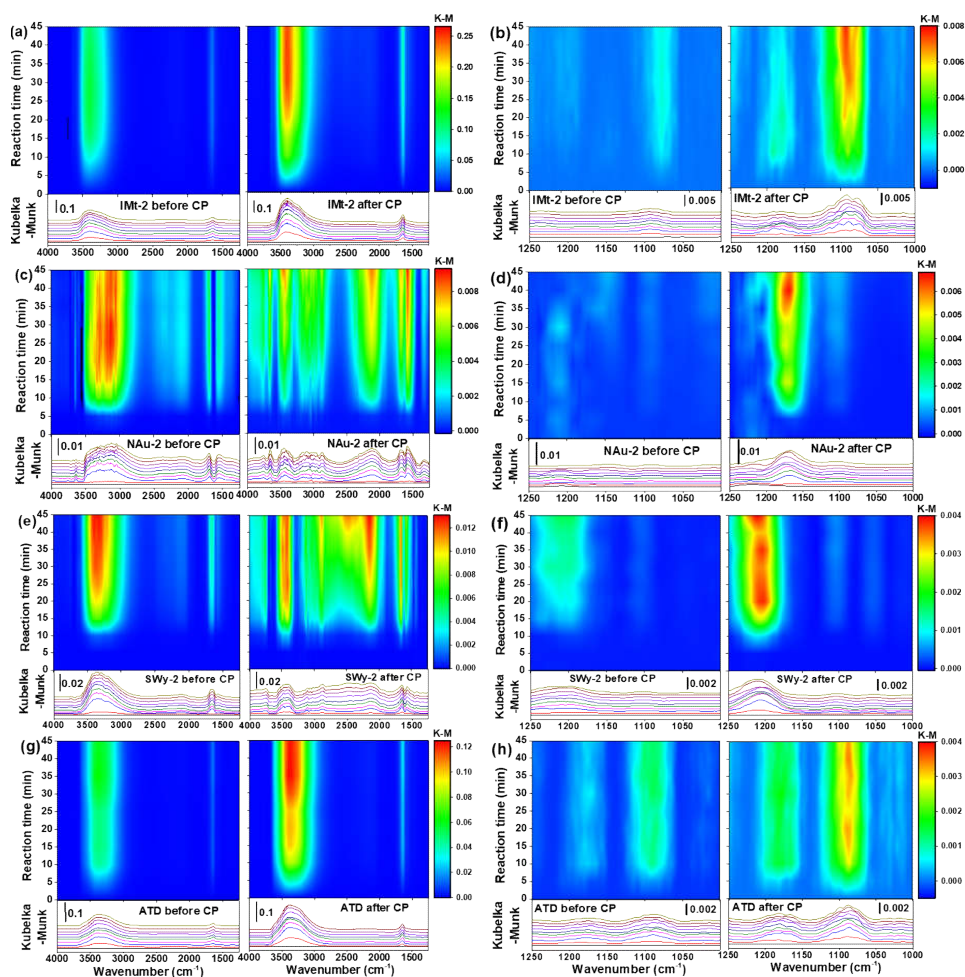




Figure 2

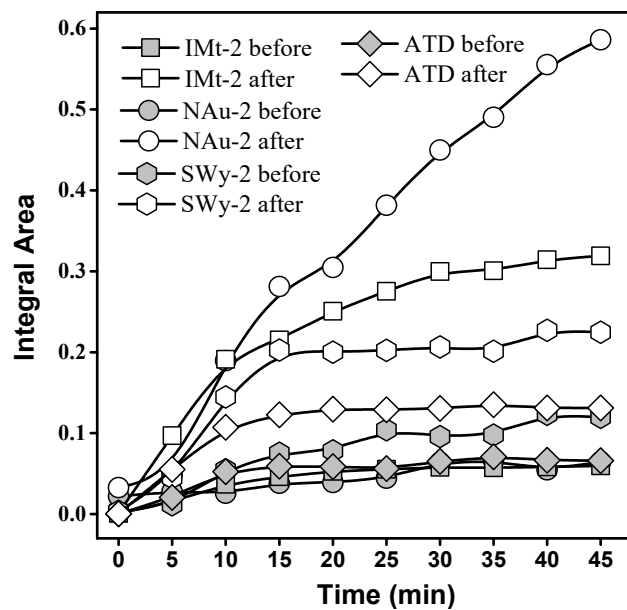




Table 1

Samples	A_{BET} ($\text{m}^2 \text{g}^{-1}$)	Sulfate formation rate (ions s^{-1}) ($\times 10^{10}$)	$A_{\text{geometric}}$ (m^2) ($\times 10^{-5}$)	γ_{BET} ($\times 10^{-12}$)	$\gamma_{\text{geometric}}$ ($\times 10^{-7}$)
IMt-2 before CP	20.1 ± 1.5	6.13	1.95	2.62	1.03
IMt-2 after CP	32.0 ± 2.6	28.72	1.95	5.76	4.85
NAu-2 before CP	19.8 ± 1.3	1.80	1.95	0.75	0.30
NAu-2 after CP	93.7 ± 7.5	34.57	1.95	3.06	5.83
SWy-2 before CP	22.6 ± 2.3	10.20	1.95	3.70	1.72
SWy-2 after CP	40.8 ± 1.5	27.19	1.95	5.49	4.59
ATD before CP	4.3 ± 0.3	8.11	1.95	16.05	1.37
ATD after CP	6.5 ± 1.0	16.33	1.95	22.33	2.76



Figure 3

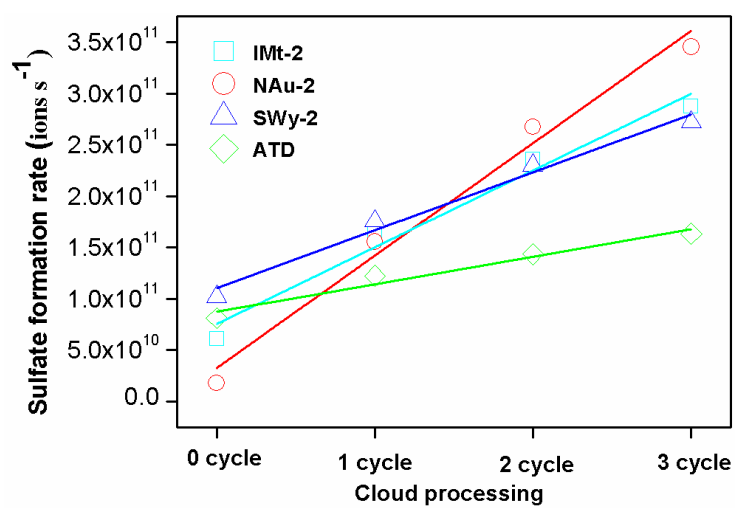




Figure 4

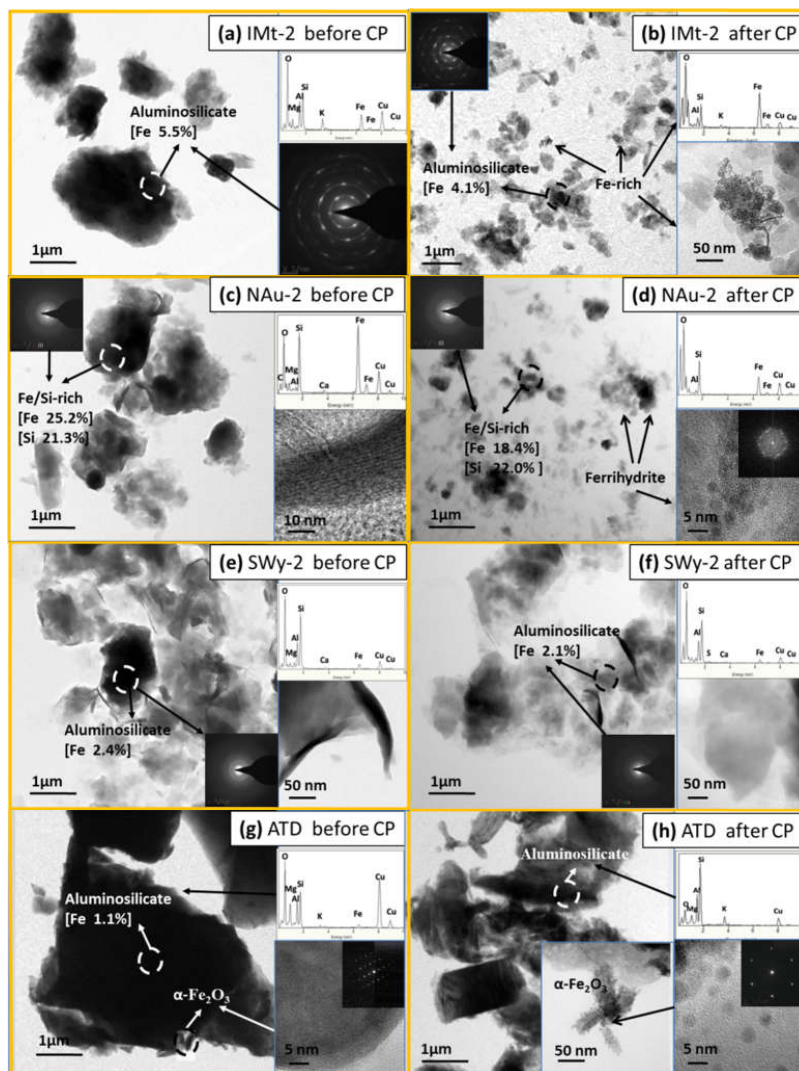




Figure 5

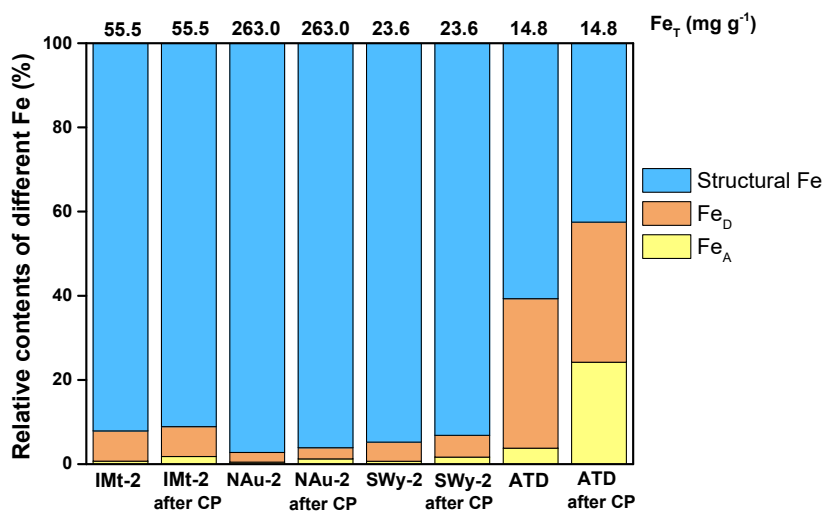




Figure 6

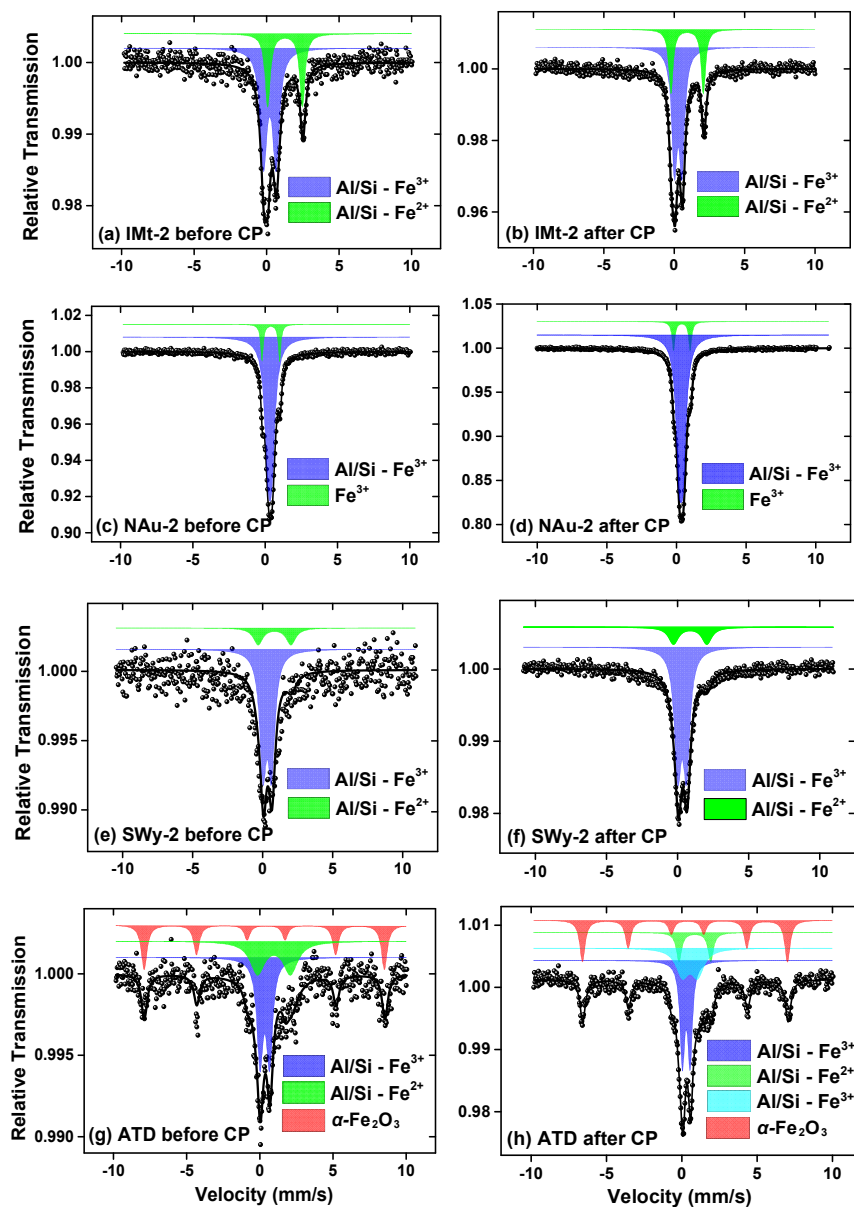




Figure 7

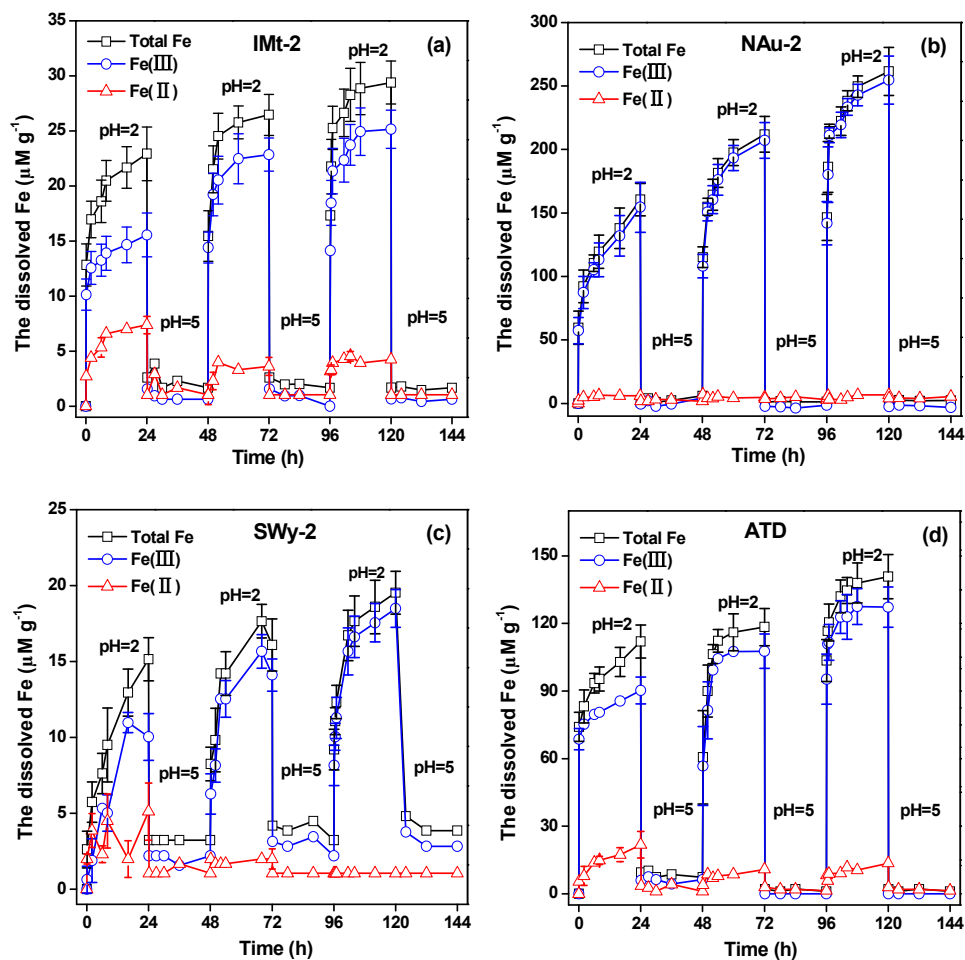




Figure 8

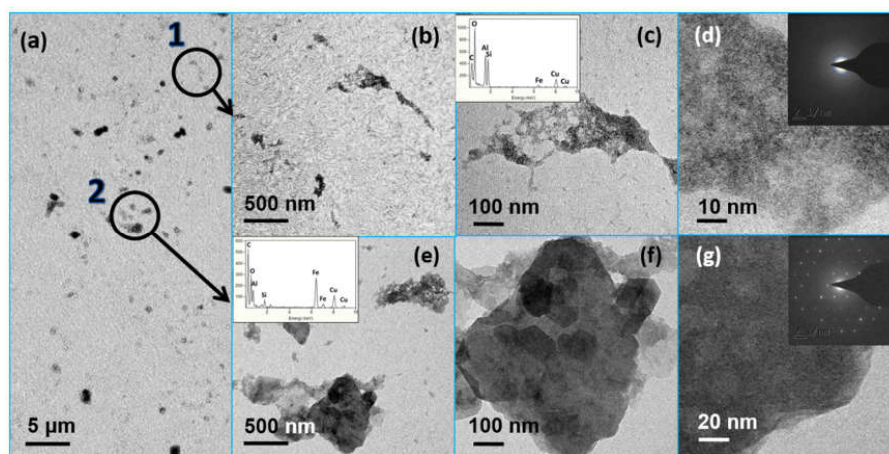




Figure 9

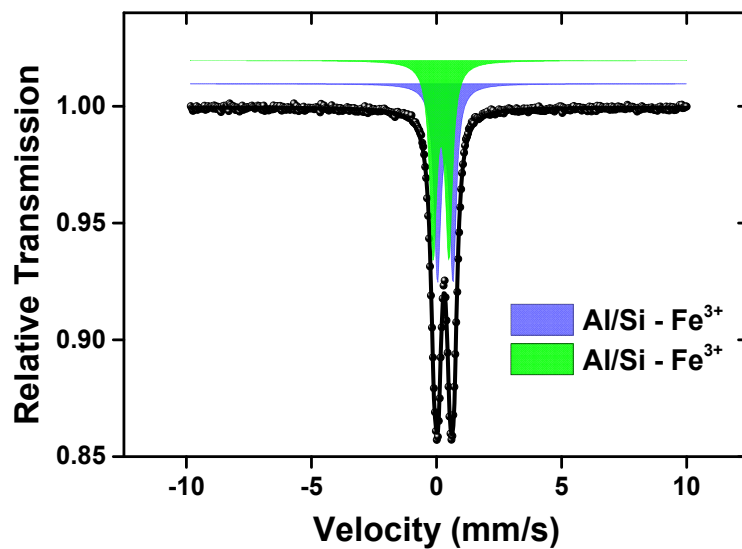




Figure 10

